INSTITUTE OF PHYSICS PUBLISHING PHYSICS IN MEDICINE AND BIOLOGY

Phys. Med. Biol. **50** (2005) 4887–4912 doi:10.1088/0031-9155/50/20/010

Statistical dynamic image reconstruction in state-of-the-art high-resolution PET

Arman Rahmim[1], Ju-Chieh Cheng[2], Stephan Blinder[3], Maurie-Laure Camborde[3] and Vesna Sossi[2]

[1] Department of Radiology, Johns Hopkins University School of Medicine, Baltimore, MD 21287, USA
[2] Department of Physics and Astronomy, University of British Columbia, Vancouver, BC V6T 1Z1, Canada
[3] Pacific Parkinson's Research Centre, Vancouver, BC V6T 1Z1, Canada

E-mail: arahmim1@jhmi.edu, jcheng@phas.ubc.ca, blinder@phas.ubc.ca, marie@pet.ubc.ca and vesna@phas.ubc.ca

Received 9 May 2005, in final form 1 August 2005
Published 5 October 2005
Online at stacks.iop.org/PMB/50/4887

Abstract

Modern high-resolution PET is now more than ever in need of scrutiny into the nature and limitations of the imaging modality itself as well as image reconstruction techniques. In this work, we have reviewed, analysed and addressed the following three considerations within the particular context of state-of-the-art dynamic PET imaging: (i) the typical average numbers of events per line-of-response (LOR) are now (much) less than unity, (ii) due to the physical and biological decay of the activity distribution, one requires robust and efficient reconstruction algorithms applicable to a wide range of statistics and (iii) the computational considerations in dynamic imaging are much enhanced (i.e., more frames to be stored and reconstructed). Within the framework of statistical image reconstruction, we have argued theoretically and shown experimentally that the sinogram non-negativity constraint (when using the delayed-coincidence and/or scatter-subtraction techniques) is especially expected to result in an overestimation bias. Subsequently, two schemes are considered: (a) subtraction techniques in which an *image* non-negativity constraint has been imposed and (b) implementation of random and scatter estimates inside the reconstruction algorithms, thus enabling direct processing of Poisson-distributed prompts. Both techniques are able to remove the aforementioned bias, while the latter, being better conditioned theoretically, is able to exhibit superior noise characteristics. We have also elaborated upon and verified the applicability of the accelerated list-mode image reconstruction method as a powerful solution for accurate, robust *and* efficient dynamic reconstructions of high-resolution data (as well as a number of additional benefits in the context of state-of-the-art PET).

(Some figures in this article are in colour only in the electronic version)

1. Introduction

In positron emission tomography (PET) systems, there is a continuous effort to increase sensitivity and to improve spatial resolution. State-of-the-art high-resolution PET, particularly in the dynamic imaging modality, is now more than ever in need of scrutiny into the nature and limitations of PET imaging and image reconstruction techniques. As a first observation, we note that the increasing number of crystals, and therefore the number of lines-of-response (LORs), in modern tomographs is now beginning to pose challenges from the data storage point of view (as further elaborated upon later). Moreover, time-complexity of image reconstruction can become particularly problematic as a consequence.

To better exemplify this, one may make the following interesting observation (Nutt 2003): the number of individual crystals in PET tomographs has doubled approximately every 2 years for the past 25 years. The corresponding number of LORs (measured by the square of the number of detector elements) has therefore grown faster compared to the available computing power as given by Moore's Law (the number of transistors in an integrated circuit doubles every 18 months). One is therefore prompted to take into consideration novel and innovative image reconstruction techniques which enable feasible processing of the full information available from state-of-the-art and next-generation scanners.

With increasing interest in dynamic PET imaging, as a powerful technique providing *in vivo* quantitative information of dynamic physiological and biochemical processes, and usually achieved via storage and reconstruction of multiple acquisition frames, two important considerations naturally arise: (i) the aforementioned storage and computational considerations are only further enhanced (i.e., more frames to be stored and reconstructed); (ii) due to the physical and biological decay of the activity distribution, the dynamic frames may span a wide range of total-count and count-rate statistics. The latter concern necessitates consideration of the robustness of the reconstruction algorithms in a wide range of statistics, especially in the context of corrections for random coincidences and scattered events, as elaborated in sections 2 and 3.

Regarding the first consideration, the introduction of the list-mode acquisition modality has proven particularly convenient and useful. List-mode acquisition is achieved by storing information regarding the acquired events as they are detected one-by-one in the form of a list. The recorded information, or *attributes* of the list-mode events, typically consist of coordinates of the two detectors along which the photons are detected in coincidence, together with the time-of-detection. It is also possible to store further attributes for each event in the list-mode data, such as information about the time-of-flight, depth-of-interaction and energy. Once the list-mode data are acquired, they can be binned and sub-divided into multiple frames of desired durations, and therefore greater utility is gained by removing the need to specify the frames in advance prior to the scan. Furthermore, in terms of the storage demand, the list-mode acquisition is particularly useful, as demonstrated below.

As a notable example, we shall focus on the high-resolution research tomograph (HRRT): a state-of-the-art octagonal-design depth-of-interaction (DOI) encoding (dual layer LSO/LYSO), 3D-only dedicated PET scanner containing a total of 119,808 detector crystals. The total number of possible LORs in the HRRT is nearly 4.5 billion, exceeding most PET scanners by 2–3 orders of magnitude. With no LOR *mashing* (i.e., no compression of neighbouring LORs), the data set for a single frame contains 10 816 sinograms (each containing 256 radial and 288 azimuthal bins) corresponding to ∼0.8 G sinogram bins (∼1.6 GB of data). Application of data mashing, on the other hand, has been shown to adversely affect image resolution, especially as one moves away from the centre of the field-of-view (FoV) (Wienhard *et al* 2002). With no data mashing in a typical histogram-mode-acquired

C-11 dynamic study, wherein the scan duration is divided into, say, 18 dynamic frames, one would obtain 18×1.6 GB $= 29$ GB of data, whereas one typically collects only around ∼5–6 GB of list-mode data.

The following important observation can be subsequently raised: in modern PET scanners, the average number of events per LOR is no longer significantly above unity. In the case of the HRRT, one typically observes 10–200M counts per frame, corresponding to only ∼0.012–0.25 average counts per sinogram bin, which remarkably emphasizes the count-limited nature of PET imaging. In other words, the (vast) majority of bins in histogrammed PET data are likely not to measure any counts. This is particularly going to be the case with next-generation time-of-flight (TOF) PET scanners (see section 4). Three important observations can be made from this:

(i) The Gaussian approximation to the Poisson nature of the detection process is very inaccurate in these scanners. This rules out (weighted) least squares image reconstruction techniques (Fessler 1994), which in the past have only been of concern in low-count studies, whereas they become categorically non-valid in state-of-the-art PET.
(ii) Correction of measured events for random coincidences and/or scattered events (via subtraction of delayed coincidences and/or estimated scatter counts) can commonly yield negative sinogram bins, which needs to be critically considered. This is elaborated in sections 2 and 3.
(iii) The sparseness of the sinogram data sets can point to an intrinsic advantage in application of list-mode image reconstruction techniques (i.e., direct processing of the list-mode-acquired events). Section 4 discusses this in detail.

It is the very aim of this work to investigate the applicabilities and limitations of various image reconstruction techniques, within the context of state-of-the-art high-resolution PET imaging. Sections 2 and 3 outline accuracy considerations for several random and scatter correction techniques in the aforementioned context of high-resolution state-of-the-art PET imaging. Sinogram versus image non-negativity constraints have meanwhile been discussed. Section 4 introduces the list-mode image reconstruction method as a technique highly suitable for state-of-the-art PET imaging, and discussed a number of variations to the list-mode technique. Details of implementation of quantitative dynamic image reconstruction, along with the study of various list-mode projection methods, have been elaborated in section 5, with the experimental methods and results presented in sections 6 and 7.

2. Random correction techniques

2.1. Subtraction of delayed coincidences

The most common technique to correct for random coincidences (*randoms*) is to acquire events (*delays*) arriving within a delayed-coincidence window, such that the probability of a true coincidence is zero (this acquisition mode is available in most modern PET scanners). The delays are similarly distributed compared to the actual randoms acquired within the true coincidence window. Thus, subtraction of the delays from the events measured within the coincidence window (*prompts*) effectively corrects (in average) for the bias introduced by the randoms. In many existing PET scanners, the prompts data are precorrected for the detection of randoms by *real-time* subtraction of the delayed coincidences prior to the reconstruction step, intended to minimize data transfer and processing times. In scanners in which the prompts and delayed coincidences are separately measured, still, a similar subtraction is commonly performed inside the reconstruction schemes. Nevertheless, the subtraction technique can be

problematic and can introduce challenges to the accuracy of the image reconstruction tasks, as we discuss next.

Denoting y_i^p and y_i^d as the number of prompts and delayed coincidences along an LOR i ($i = 1, \ldots, I$), one performs $y_i = y_i^p - y_i^d$ to obtain randoms-precorrected data. Commonly, y_i is approximated as a Poisson variable also (see below for further discussion), and one chooses to maximize, with respect to the image vector $\vec{\lambda} = [\lambda_1 \cdots \lambda_J]^T$, the Poisson log-likelihood function

$$l(\vec{\lambda}) = \sum_{i=1}^{I} \{-\bar{y}_i(\vec{\lambda}) + y_i \ln \bar{y}_i(\vec{\lambda})\} \tag{1}$$

where

$$\bar{y}_i(\vec{\lambda}) = \bar{n}_i + \bar{s}_i = \sum_{j=1}^{J} p_{ij}\lambda_j + \bar{s}_i \tag{2}$$

is the sum of the expected number of trues $\bar{n}_i$ and scattered events $\bar{s}_i$ along the LOR i. As a first observation, we note that y_i can exhibit a negative value. In other words, taking the variable Y_i to denote the precorrected counts along a particular LOR i, and defining $\bar{y} = \bar{n}_i + \bar{s}_i$ and $\bar{r}$ as the expected number of randoms-corrected prompts (trues + scatter) and randoms, respectively, Y_i has a distribution given by

$$Y = \text{Poisson}\{\bar{y} + \bar{r}\} - \text{Poisson}\{\bar{r}\}. \tag{3}$$

Clearly, while $E\{Y_i\} = \bar{y}_i$ is non-negative, the Poisson nature of the individual prompts and delayed measurements can result in negative y_i values.

We next note that in the simple case where $\bar{s}_i$ has a value of 0, negative y_i values could cause a reconstruction algorithm that maximizes the likelihood function (1) to diverge, since $l(\vec{\lambda}) = +\infty$ for $y_i < 0$ and $\bar{n}_i = 0$. Conventionally, zero thresholding has been used (Michel *et al* 1998, 1999) to address this problem, wherein one maximizes the following log-likelihood function:

$$l(\vec{\lambda}) = \sum_{i=1}^{I} \{-\bar{y}_i(\vec{\lambda}) + [y_i]_+ \ln \bar{y}_i(\vec{\lambda})\} \tag{4}$$

where $[y_i]_+ = y_i$ if $y_i > 0$ and is 0 otherwise. The function can for instance be maximized using the EM algorithm (incorporating sinogram non-negativity):

$$\lambda_j^{m+1} = \frac{\lambda_j^m}{\sum_{i=1}^{I} p_{ij}} \sum_{i=1}^{I} p_{ij} \frac{[y_i]_+}{\sum_{b=1}^{J} p_{ib}\lambda_b^m + \bar{s}_i} \tag{5}$$

where λ_j^m denotes the image intensity in voxel j ($j = 1, \ldots, J$) at the mth iteration and p_{ij} is the probability of an emission from voxel j being detected along LOR i ($i = 1, \ldots, I$).

Nevertheless, this approach is bound to result in a positive systematic bias (Ahn and Fessler 2004, Bélanger *et al* 2004), especially in high-resolution tomographs. To see this more elaborately, we note that Y can be shown (Yavuz 1999) to have a probability mass function given by

$$P(Y = y|\bar{y}) = \frac{e^{-(\bar{y}+2\bar{r})}}{i^{|y|}} \left(\sqrt{\frac{\bar{y}+\bar{r}}{\bar{r}}}\right)^{y} J_{|y|}\left(2i\sqrt{(\bar{y}+\bar{r})\bar{r}}\right) \tag{6}$$

where $J_n(\cdot)$ is the Bessel function of the first kind of order n and $i = \sqrt{-1}$. Examples of this ($\bar{y} = 0.1, 1.0, 10$ with $\bar{r} = 20\%$) are depicted in figure 1(a). Clearly, with a scanner exhibiting average-counts-per-LOR of $\sim$1 (and less), one would expect significant bias to be

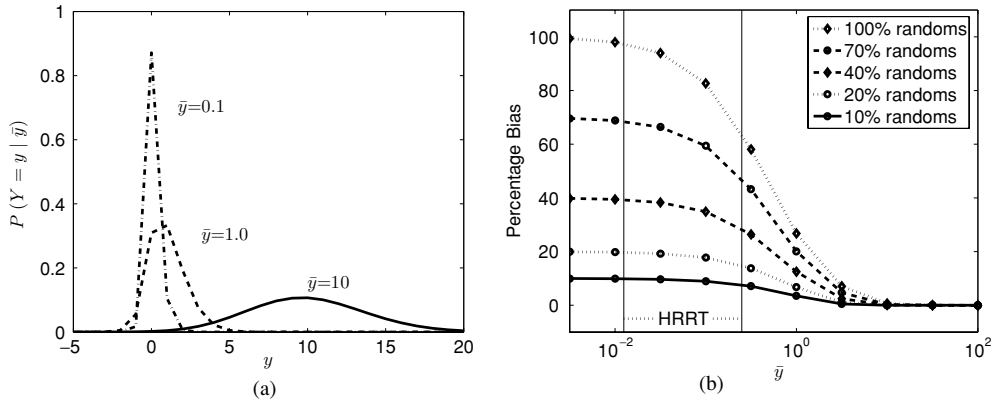

Figure 1. (a) The probability $P(Y = y|\bar{y})$ as a function of y (random fraction is 20%). (b) Percentage bias due to zero thresholding in subtraction of delayed coincidences.

observed if a sinogram non-negativity constraint is imposed. More quantitatively, let us define the percentage bias (PB) as

$$\mathrm{PB} = \left(\frac{E\{[Y]_+\}}{\bar{y}} - 1 \right) \times 100 \tag{7}$$

Figure 1(b) shows plots of the calculated PB for a wide range of random fractions. Clearly, for average-counts-per-LOR lower than 10, the zero-thresholding effect becomes noticeable. For the typical range of average-counts-per-LOR encountered in a state-of-the-art scanner such as the HRRT (as indicated in the plot), the sinogram non-negativity constraint is then clearly expected to result in an overestimation bias.

2.2. Sinogram versus image non-negativity constraints

In order to reduce the aforementioned systematic bias, one may replace the sinogram non-negativity constraint in the EM algorithm (5) with a milder *image* non-negativity constraint (Rahmim *et al* 2004):

$$\lambda_j^{m+1} = \frac{\lambda_j^m}{\sum_{i=1}^I p_{ij}} \left[\sum_{i=1}^I p_{ij} \frac{y_i}{\sum_{b=1}^J p_{ib}\lambda_b^m + \bar{s}_i} \right]_+ . \tag{8}$$

To see how this latter algorithm can significantly reduce the positive bias, let us consider the example of a sphere of diameter D. Using a tube-intersection model for the system matrix $P = (p_{ij})_{I\times J}$, a single back-projection will typically contribute to a small cylindrical collection of voxels, volume of which (inside the object) is approximately given by $\pi(d/2)^2 D$ (d being the diameter of the tube). This means that in an image update (with N measured events), a voxel inside the object receives of the order of M contributions:

$$M = N \frac{\text{volume of LOR intersection}}{\text{volume of object}} = N \frac{\pi\left(\frac{d}{2}\right)^2 D}{\frac{4}{3}\pi\left(\frac{D}{2}\right)^3} = N\frac{3d^2}{2D^2}. \tag{9}$$

As a simplified example for the HRRT scanner, using $D = 15$ cm and $d = 2.5$ mm, in a typical accelerated EM reconstruction process, wherein of the order of $\sim 10^6$ counts are back-projected per subset, a voxel inside the object is expected to receive $M \sim 400$ contributions. This is >3 orders of magnitude larger than the typical average number of counts acquired per sinogram

bin in the HRRT, and is expected (figure 1) to nearly eliminate the positive systematic bias. In other words, the fact that an LOR back-projection is most typically mapped onto many voxels, as well as the smaller size of the image space compared to the projection space (e.g., in the HRRT one has $\sim 14M$ image voxels compared to ~ 0.8 G sinogram bins), imply that the image voxels can receive orders of magnitude larger number of back-projected counts, and are therefore not likely to exhibit an overestimation bias when using an image non-negativity constraint. We have also experimentally validated this to be the case, as shown in section 7.

In Ahn and Fessler (2004), Ahn and Fessler have derived a separable paraboloidal surrogates (SPS) algorithm as well an EM–ML algorithm, both of which monotonically maximize the Poisson likelihood function (1) allowing negative sinogram values. However, both algorithms can be very expensive to implement. For instance, the proposed ML-EM algorithm is given by

$$\lambda_j^{m+1} = \frac{\lambda_j^m}{s_j(\vec{\lambda}^m)} \sum_{i=1}^{I} p_{ij} \frac{[y_i]_+}{\sum_{b=1}^{J} p_{ib}\lambda_b^m + \bar{s}_i} \tag{10}$$

where

$$s_j(\vec{\lambda}^m) = \sum_{i=1}^{I} p_{ij} \left(1 + \frac{[-y_i]_+}{\sum_{b=1}^{J} p_{ib}\lambda_b^m + \bar{s}_i} \right). \tag{11}$$

Note that for a scan in which $y_i \geqslant 0$ for all i, the above algorithm simplifies to the regular EM algorithm in which $s_j = \sum_{i=1}^{I} p_{ij}$. Otherwise, we note that the sensitivity correction factor $s_j(\vec{\lambda}^m)$ depends on the image estimate, and therefore needs to be updated after *every* subset. This can especially prove very time-consuming in dynamic studies (wherein by comparison the regular EM algorithm calculates s_j values only once for the entire scan and uses them subsequently in all the subsets of all the dynamic frames).

There exist a number of other approaches in the literature developed to reconstruct randoms-precorrected data. These include:

(i) *Shifted-Poisson approximation*. This technique makes note of the fact that Y in equation (3) is not a Poisson variable (e.g., note the inequality of mean and variance: $E\{Y\} = \bar{y}$, $\mathrm{Var}\{y\} = \bar{y} + 2\bar{r}$), and instead makes the approximation that $Y' = Y + 2\bar{r}$ is Poisson distributed (note the equality $E\{Y'\} = \mathrm{Var}\{Y'\} = \bar{y} + 2\bar{r}$ where we have used $\mathrm{Var}\{\bar{r}\} = 0$) (Yavuz and Fessler 1996).

(ii) *Saddle-point approximation*. This technique is obtained by a second-order Taylor series expansion (in the z-transform domain) of the log-likelihood function $l(\vec{\lambda}) = \sum_{i=1}^{I} \ln P\ (Y_i = y_i|\bar{y}_i)$ where the exact probability function is given by equation (6). The reader is referred to Snyder *et al* (1995) and Yavuz and Fessler (1998) for more detail. According to Ahn and Fessler (2004), to date, the saddle-point approach has been able to outperform other approaches to reconstruction of randoms-precorrected data.

The two aforementioned techniques are particularly suited for scanners in which randoms-precorrection is automatically performed and they require calculation of the expected random counts $\bar{r}_i$ for all the LORs (e.g., using the measured singles rates). As such, they are not optimal for reconstruction of data from scanners in which the prompts and delayed coincidences are recorded separately; they do not pose a computational advantage over the ordinary Poisson (OP) modelling of the prompts data (discussed in section 2.3), while also keeping in mind that they are approximate techniques and may require non-negativity constraints[4].

[4] For instance, in the shifted-Poisson technique, the variable $Y + 2\bar{r}$ can in fact be negative (though less likely than Y itself to be negative). The interested reader should consult Ahn and Fessler (2004) for more discussion.

(iii) *The AB-EMML algorithm.* Developed by Byrne (1998), this algorithm is an extension of EM–ML allowing the user to include prior information about the lower and upper bounds for the image values (A and B in AB-EMML stand for these bounds). The AB-EMML algorithm has previously been applied to SPECT imaging[5]. The algorithm converges to the solution of $\vec{y} = P\vec{\lambda}$ while satisfying the vector inequalities $\vec{A} \leqslant \vec{\lambda}_i \leqslant \vec{B}$, when such a solution exists (consistent case). In the realistic (inconsistent) case, the algorithm converges to a solution which minimizes a cost function related to the so-called Kullback–Leibler (KL) cross-entropy[6]. Considering a negative lower bound only (i.e., setting $\vec{B} = +\infty$), it is possible to show that the AB-EMML algorithm can be re-written in the form

$$\lambda_j^{m+1} = -|A_j| + \frac{\lambda_j^m + |A_j|}{\sum_{i=1}^{I} p_{ij}} \sum_{i=1}^{I} p_{ij} \left[\frac{y_i + |P\vec{A}|_i}{\bar{y}_i(\vec{\lambda}^m) + |PA|_i} \right] \tag{14}$$

where $\bar{y}_i(\vec{\lambda}^m)$ is the expected number of (randoms-precorrected) counts, given by equation (2). The algorithm can be shown to converge to a minimizer of the cost function $KL(\vec{y} + |P\vec{A}|, P\vec{\lambda} + |P\vec{A}|)$, which is equivalent to maximizing the log-likelihood function

$$l(\vec{\lambda}) = \sum_{i=1}^{I} \{-(\bar{y}_i + |P\vec{A}|_i) + (y_i + |P\vec{A}|_i) \ln(\bar{y}_i + |P\vec{A}|_i)\}. \tag{15}$$

This technique (compared to the aforementioned two methods) does not require measurement/calculation of the expected random counts $\bar{r}_i$. Yet, it effectively assumes $Y_i' = Y_i + |P\vec{A}|_i$ to be Poisson distributed, and in this sense, is a less accurate model than, for instance, the shifted-Poisson approximation which is specifically tuned to match the mean and variance of the randoms-precorrected data (using the variable $Y_i' = Y_i + 2\bar{r}_i$).

2.3. Direct reconstruction from prompts data

There are two important advantages in avoiding altogether the delayed-coincidence subtraction technique:

(i) As already noted, the subtraction technique, while compensating in mean for the presence of randoms, increases the variance of the data. This is the very reason why the noise equivalent count (NEC) rate, as a function of the true, scatter and random event rates (R_t, R_s and R_r) is given by Daube-Witherspoon *et al* (2002)

$$\text{NEC} = \frac{R_t^2}{R_t + R_s + kR_r} \qquad \text{where} \quad k = \begin{cases} 2 & \text{delayed subtraction} \\ 1 & \text{otherwise} \end{cases} \tag{16}$$

[5] Erlandsson *et al* (2000) use the AB-EMML (with $A < 0$) in order to allow for negative image values in low-statistic (dynamic) SPECT, which can yield negative projections after correction for scatter. In a different context, Narayanan *et al* (1999) use this algorithm ($A < 0$) in an application of the Karhunen–Loeve (KL) transform to 4D reconstruction of cardiac gated SPECT images (thus accounting for negative values in the KL space). On the other hand, Kohli *et al* (1999) use *positive* lower and upper bounds, to accelerate resolution recovery in cardiac SPECT.

[6] The cross-entropy or KL distance between two i-dimensional vectors is given by

$$\text{KL}(\vec{M}, \vec{N}) = \sum_{i=i}^{I} \left\{ N_i - M_i + M_i \ln \frac{M_i}{N_i} \right\}. \tag{12}$$

When minimizing, for instance, $\text{KL}(\vec{y}, P\vec{\lambda})$ with respect to $\vec{\lambda}$ (first term independent of the parameter being estimated), the task can be seen to be equivalent to maximizing the Poisson log-likelihood function

$$l(\vec{\lambda}) = \sum_{i=1}^{I} \{-(P\vec{\lambda})_i + y_i \ln(P\vec{\lambda})_i\}. \tag{13}$$

wherein it is implicitly noted that the subtraction of delayed coincidences degrades the signal-to-noise ratio.

(ii) All the aforementioned algorithms, which have been developed to tackle data that are precorrected using the delayed-coincidence events, are approximate in nature (with the exception of the computationally expensive equation (10)). In contrast, the direct reconstruction of the prompts data does not require such approximations. To see this we note that the prompts data y_i^p are themselves Poisson distributed, having an *exact* ordinary Poisson (OP) log-likelihood objective function:

$$l(\vec{\lambda}) = \sum_{i=1}^{I} \left\{ -\bar{y}_i^p(\vec{\lambda}) + y_i^p \ln \bar{y}_i^p(\vec{\lambda}) \right\} \tag{17}$$

where

$$\bar{y}_i^p(\vec{\lambda}) = \bar{n}_i + \bar{r}_i + \bar{s}_i = \sum_{j=1}^{J} p_{ij}\lambda_j + \bar{r}_i + \bar{s}_i. \tag{18}$$

Application of expectation maximization, for instance, yields the following OP-EM algorithm (Politte and Snyder 1991):

$$\lambda_j^{m+1} = \frac{\lambda_j^m}{\sum_{i=1}^{I} p_{ij}} \sum_{i=1}^{I} p_{ij} \frac{y_i^p}{\sum_{b=1}^{J} p_{ib}\lambda_b^m + \bar{r}_i + \bar{s}_i}. \tag{19}$$

In this approach, one does require knowledge of the expected random rates (which was also the case for the shifted-Poisson and saddle-point approximations). To address this issue, two approaches are possible: (i) using singles measurements at the detectors (Rokitta *et al* 2000) to calculate the expected randoms contribution or (ii) variance reduction (smoothing) for the measured delayed events (Casey and Hoffman 1986, Mumcuoğlu *et al* 1996a, Badawi *et al* 1999).

The first approach has the advantage of utilizing high statistics singles measurements. At the same time, it increases the 'bandwidth' of the scanner, since delayed time windows need not be imposed for delayed-coincidence measurements, and thus less saturation of counts would occur especially for studies involving high count rates. In the particular case of the HRRT scanner, however, the singles rates can *only* be measured at the block level and *not* for the individual crystals. This can result in a relatively coarse estimation of the random rates at the individual crystals. One possible approach is to introduce and measure relative efficiency factors for the individual crystals within a block; however, these factors are found to be count-rate dependent (Barker *et al* 2004).

An alternative approach, currently available for the HRRT scanners and used in this work, involves a generalization of the Casey 3D random-smoothing technique (Casey and Hoffman 1986) and estimates the crystal singles rates from the delayed-coincidence measurements (inherently including the effect of dead time) followed by a standard calculation of the random rates from the singles.

3. Calculation of scattered events

Of the various scatter-correction techniques (e.g., convolution-subtraction (Bailey and Jones 1994, Reader *et al* 2001), comparison of 2D and 3D distributions (Cherry *et al* 1993), dual energy-window acquisition methods (Grootoonk *et al* 1996) and direct calculation of the scatter distribution using the Klein–Nishina formula (Ollinger 1996)), the latter type of calculation is attractive since it treats the scatter using basic physical principles and is gradually becoming a practical alternative due to increasing computing power. In the present study, we have used the

Watson single scatter simulation (SSS) technique (Watson 2000). The original implementation of the algorithm was purely image based (i.e., would compute the scatter contribution using *only* an initial image estimate, followed by a subtraction in image space). More recent versions (Watson 2003) utilize the histogrammed data additionally to scale the calculated scattering components in order to compensate for external scatter.

The nonlinearity of statistical reconstruction methods such as the EM algorithm, as opposed to the analytic techniques, implies that the subtraction of scatter in image space is not an accurate approach. Alternatively, in the present context of dynamic high-resolution PET imaging, we have investigated quantitative accuracies associated with two commonly employed scatter-correction schemes.

(i) *Subtraction of scatter in projection space*. This method involves the subtraction of estimated scattered events $\bar{s}_i$ from the measured events along each LOR i. The approach has a potential limitation: it can be seen to be problematic in a very similar sense to the subtraction technique for the delayed coincidences. To see this, let us neglect random events momentarily and choose the variable Y_i to denote the measured counts along an LOR i:

$$Y_i = \text{Poisson}\{\bar{n}_i + \bar{s}_i\} - \bar{s}_i. \tag{20}$$

One may then note that this distribution (i) does not follow Poisson statistics (e.g., note the inequality of mean and variance: $E\{Y\} = \bar{n}$, $\text{Var}\{Y\} = \bar{n} + \bar{s}$) and (ii) may result in negative values, the former challenging the accuracy of the EM reconstruction task and the latter forcing the introduction of non-negativity constraints (and the various complications, as discussed in section 2.2).

(ii) *Inclusion of scatter inside the reconstruction algorithm.* Considering the OP-EM algorithm (19), the calculated $\bar{s}_i$ values are used in the denominator of the EM algorithm, along with the expected trues and randoms, to provide an expected value for the number of prompts measured along an LOR i (in the numerator). This approach, unlike the scatter precorrection method, maintains the Poisson nature of the data and does not require application of non-negativity constraints[7].

It must be noted here that the aforementioned scatter-correction techniques, though very commonly employed in the literature, are technically not exact, since strictly speaking they require access to the true image (which is the very task at hand) in order to calculate the estimated scattered events. In practice, this is achieved by an initial fast reconstruction of the image.

An alternate technique involves inclusion of the effect of scatter *directly* into the system matrix $P = (p_{ij})_{I \times J}$. In this way, one would be computing the *probability* that an annihilation generated in a voxel j would be detected along an LOR i, including the effect of scatter. This technique therefore *only* requires access to the attenuation data, and is independent of the emission image, and is in this sense exact as it does not require an initial estimate for the emission image. However, the extension of this technique from 2D (Markiewicz *et al* 2004, Tamal *et al* 2004) to 3D PET, especially in state-of-the-art PET, is very complex as it renders the system matrix very non-sparse (highly complicating on-the-fly calculations) and scan-specific (not allowing pre-calculation of a look-up table), and remains to be investigated in future studies.

[7] As an additional note: in order to speed up the convergence of OP-EM, the scatter (and smoothed random estimates) are introduced into the image update factor starting with the second subset. It was in fact found that the image estimate 'updates' itself much more quickly in the denominator of the subsetized EM algorithm without the scatter and random estimates. The image estimate, obtained from the first subset, will thus be more quantitatively commensurate with respect to the expected scatter and random estimates.

4. List-mode image reconstruction

As elaborated in section 1, state-of-the-art high resolution PET imaging, particularly in the dynamic imaging modality, can require processing of very large data sets. As we describe below, the list-mode image reconstruction method provides a very practical solution for efficient and accurate reconstructions. These, in addition to other advantages of the technique, are discussed below.

4.1. The technique and its benefits

Conventional image reconstruction techniques histogram the collected data into sinogram bins. This can be achieved by (i) direct histogram-mode data acquisition or (ii) by histogramming data initially collected in the list-mode acquisition modality (as introduced in section 1). Nevertheless, we elaborate on several benefits that can be gained by direct reconstruction of the individual list-mode data events (i.e., bypassing the histogramming step).

(i) *Faster reconstruction.* As elaborated in section 1, in modern PET imaging, the average number of events measured per LOR is becoming (much) less than unity. List-mode reconstruction techniques implicitly ignore LORs along which counts are not recorded (Reader *et al* 1998) and can therefore (considerably) improve the reconstruction speed.

(ii) *Preservation of maximum sampling frequency.* When histogram-mode reconstruction methods are used, the data are often *mashed*, i.e. certain 'nearby' LORs are histogrammed into the same sinogram bin in order to reduce the size of the sinogram data. Application of data mashing, however, degrades the image resolution, especially away from the centre of the FoV (Wienhard *et al* 2002). In the case of list-mode reconstruction, since events are considered one-by-one, sinogram data compression is in principle not needed, thus resulting in preservation of maximum sampling frequency at no extra cost.

(iii) *Time-of-flight PET.* With the continuous improvements in the technology of PET imaging (e.g., faster electronics, discovery of the scintillator LSO), time-of-flight (TOF) PET is now being actively reconsidered (Moses 2003). TOF PET, especially in whole body scanning, is expected to considerably improve image noise behaviour (Kimdon *et al* 2003). The important observation is that with the added attribute of TOF measured for the acquired events, increasingly more sinogram bins will be required to take into account the measured TOF information along each LOR. In contrast, with list-mode reconstruction, one does not require the use of sinogram bins and instead processes the events one-by-one, conveniently including the TOF information for each event.

(iv) *Accuracy and convenience of motion correction.* High resolution clinical imaging may only be achieved after implementation of accurate and practical motion compensation methods, for which the list-mode approach is particularly suited. In histogram-mode reconstruction, a motion-corrected LOR will not typically correspond exactly to the centre of a sinogram bin and therefore an interpolation needs to be performed (figure 2(a)). In list-mode reconstruction, however, motion-corrected list-mode event coordinates can be maintained as continuous variables (Rahmim *et al* 2004), thus preserving a higher degree of accuracy in the reconstruction task. This points to a potential advantage in terms of better sampling of the motion-corrected data in list-mode reconstruction. Furthermore, in histogram-mode reconstruction, the regularly employed sinogram space has to be extended in order to allow histogramming of *all* motion-compensated LORs including those that do not correspond to existing detector pairs (figure 2(b)), a problem again not encountered in list-mode reconstruction (Rahmim *et al* 2004).

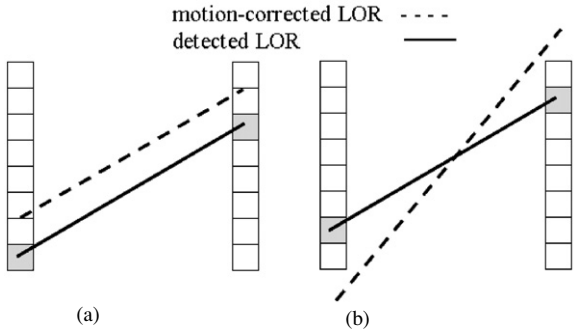

Figure 2. In histogram-mode reconstruction: (a) a motion-corrected LOR needs to be interpolated into sinogram bins. (b) The sinogram space also needs to be extended in order to allow histogramming of motion-corrected LORs that do now correspond to actual detector pairs.

(v) *Spatio-temporal reconstruction*. Another interesting possibility with list-mode data is that of truly 4D image reconstruction. This approach would *not* consist of dividing the data into multiple frames (activities within which are assumed to be static). Rather, it would involve the use of temporal basis function to represent the activity in each voxel and estimating the coefficients of the basis functions by the *collective* use of the data. We plan to explore and investigate this exciting possibility in future works. A possible approach has already been presented by Nichols *et al* (2002).

4.2. List-mode EM reconstruction

The list-mode expectation maximization (LMEM) reconstruction algorithm has been elaborated elsewhere (see, e.g., Parra and Barrett (1998), Reader *et al* (2002), Rahmim *et al* (2004)). Here, we briefly summarize the EM schemes that have been investigated in this work. The general LMEM algorithm can be written as

$$\lambda_j^{m+1} = \frac{\lambda_j^m}{\sum_{i=1}^{I} p_{ij}} \sum_{k=1}^{N} p_{i_k j} \frac{1}{\sum_{b=1}^{J} p_{i_k b} \lambda_b^m} \tag{21}$$

where i_k refers to the LOR along which the kth list-mode event is detected and n is the number of measured events. Including the effects of randoms and scattered events, the random subtraction RS-LMEM algorithm (including an image non-negativity constraint) can be written as

$$\lambda_j^{m+1} = \frac{\lambda_j^m}{\sum_{i=1}^{I} p_{ij}} \left[\sum_{k=1}^{N} p_{i_k j} \frac{\delta_k}{\sum_{b=1}^{J} p_{i_k b} \lambda_b^m + \bar{s}_{i_k}} \right]_+ \tag{22}$$

where

$$\delta_k = \begin{cases} 1 & k \text{ is a prompt event} \\ -1 & k \text{ is a delayed-coincidence event} \end{cases} \tag{23}$$

which can be seen (Rahmim *et al* 2004) to be equivalent to the histogram-mode algorithm (8). As noted at the beginning of section 3, this work uses the single scatter simulation (SSS) method to create an estimated scatter sinogram used in both histogram-mode and list-mode techniques. In list-mode reconstruction, once processing a given event k, the scatter

contribution is looked up from the scatter sinogram bin corresponding to LOR i_k. Similarly, the ordinary Poisson OP-LMEM algorithm has the form

$$\lambda_j^{m+1} = \frac{\lambda_j^m}{\sum_{i=1}^{I} p_{ij}} \sum_{k=1}^{N} p_{i_k j} \frac{1}{\sum_{b=1}^{J} p_{i_k b} \lambda_b^m + \bar{r}_{i_k} + \bar{s}_{i_k}} \tag{24}$$

and requires, in contrast to the RS-LMEM scheme, access to the *estimated* randoms for the LORs.

4.3. Accelerated list-mode reconstruction

The use of subsets, as originally employed by Hudson and Larkin (1994) in the histogram-mode ordinary subset EM (OSEM) algorithm, is similarly applicable to list-mode image reconstruction (Reader *et al* 1998): in this case, the subsets are event based (instead of LOR based) and are obtained by sub-dividing the list-mode data into segments that span a fraction of the total duration. We shall use S_l to denote the lth list-mode subset ($l = 1, \ldots, L$) and $\lambda_j^{m,l}$ as the image estimate at voxel j ($l = 1, \ldots, J$) at the mth iteration and lth subset. The subsetized list-mode expectation maximization (S-LMEM) algorithm is then given by

$$\lambda_j^{m,l} = \frac{\lambda_j^{m,l-1}}{\sum_{i=1}^{I} p_{ij}} \sum_{k \in S_l} p_{i_k j} \frac{1}{\sum_{b=1}^{J} p_{i_k b} \lambda_b^{m,l-1}} \tag{25}$$

wherein random and scatter-correction factors can be easily incorporated (RS- and OP-LMEM).

It must be noted that the regularly subsetized EM algorithm (histogram mode or list mode) is not a mathematically convergent algorithm and can result in limit cycles (Rahmim *et al* 2004), though in practice it is seen to perform considerably faster than the non-subsetized algorithm. We have therefore additionally considered a convergent subsetized list-mode EM (CS-LMEM) algorithm (Khurd and Gindi 2003, Rahmim *et al* 2004), which follows very similarly the convergent C-OSEM approach by Hsiao *et al* (2002a, 2002b). It can be written as

$$\tilde{\lambda}_j^{m,l} = \frac{\lambda_j^{m,l-1}}{\sum_{i=1}^{I} p_{ij}} \sum_{k \in S_l} p_{i_k j} \frac{1}{\sum_{b=1}^{J} p_{i_k b} \lambda_b^{m,l-1}} \tag{26}$$

$$\lambda_j^{m,l} = \sum_{s=1}^{l} \tilde{\lambda}_j^{m,s} + \sum_{s=l+1}^{L} \tilde{\lambda}_j^{m-1,s} \tag{27}$$

where $\tilde{\lambda}_j^{m,l}$ is an *intermediate* image vector produced by the first update (equation (26)), subsequently used by equation (27) to arrive at the overall image estimate $\lambda_j^{m,l}$. The algorithm takes the form of additive updates in image space, in that upon arriving at any subset, the intermediate image updates for previous subsets are added to the update for the current subset.

It must however be noted that the additive nature of the algorithm makes the update scheme rather conservative and can yield considerably slow convergence rates compared to the ordinary subsetized technique. A hybrid method, starting with the ordinary subsetized algorithm and subsequently switching to the convergent algorithm, was suggested in Rahmim *et al* (2004). However, in the current work, as demonstrated in section 7, we have observed the convergence rate to be sufficiently slow even in the ordinary subsetized algorithm such that, given the practical consideration of performing less than ten iterations per frame, using the convergent algorithm was not perceived to be of much advantage.

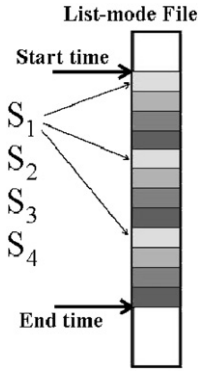

Figure 3. The frames are divided into, say, three segments, and each segment is in part divided into L portions (L being the number of data subsets).

5. Details of implementation

5.1. Quantitative dynamic image reconstruction

Our dynamic image reconstruction scheme consists of dividing the list-mode-acquired data set into specified dynamic frames, with the activities within each separately reconstructed. It must be noted here that the activity distribution (within the duration of each frame) is likely not to remain entirely static, and thus use of sequential time subsets is not desirable. In other words, one wishes to minimize differences between the maximum likelihood estimators for the various subsets by minimizing inconsistencies between the activity distributions for the subsets. We have thus used an alternative scheme for the definition of the subsets (refer to figure 3) in which each frame is divided into a number of segments, each of which is in part divided into L portions (L being the number of data subsets).

The estimated random $\bar{r}$ and scatter $\bar{s}$ contributions were calculated using the generalized Casey random-smoothing and the Watson single scatter simulation (SSS) methods, respectively, as described at the end of section 2.3 and beginning of section 3.

It must be noted here that statistical image reconstruction allows the modelling and incorporation of various physical effects into the system-matrix formulation, including effects of detector normalization and attenuation (Hebert and Leahy 1990) (included in this work) as well as positron range, non-collinearity of the annihilation photons, detector blurring and crystal penetration (e.g., see Mumcuoğlu *et al* (1996b) and Leahy and Qi (2000)). The latter effects have not been fully incorporated in this work yet, as the enormous size of the HRRT's system matrix has prompted us to adapt the approach of calculating the required system-matrix elements *on-the-fly*. A possible approach in the list-mode scheme has been presented by Reader *et al* (2002) but the authors model detector blurring/penetration effects in the image domain, which is not an accurate approach in space-variant scanners.

In the current implementation, the sensitivity correction factors, though computationally complex as they require back-projection of all possible LORs (along with normalization and attenuation factors), need only be calculated once for the entire dynamic image reconstruction task. This is because the sensitivity factors are independent of the emission scan. In the context of motion-correction EM algorithm for the HRRT, Carson *et al* (2003) have suggested sampling of a randomized portion of the LOR space for the calculation of the sensitivity factors. It remains to investigate the presence of reconstruction artefacts in this approach,

especially as it has been shown (Qi and Huesman 2003) that errors in the sensitivity image can be highly propagated into the reconstruction task[8].

5.2. List-mode projection techniques

In general, forward- and back-projection schemes can be performed using two main approaches: voxel[9]-driven and LOR-driven. It has been suggested (Egger 1996, Wallis and Miller 1997, Reader 1999) that best results may be obtained when the back- and forward-projection operations are *output-driven*, i.e. if back-projecting, the process should be voxel-driven and if forward-projecting, the process should be LOR-driven. A hand-waiving argument has been put forth (Wallis and Miller 1997): if a projection is output-driven, the operation would be a 'many-to-one' operation rather than a 'one-to-many' value operation. For instance, when back-projecting, an LOR-driven approach measures how each LOR contributes to all the voxels ('one-to-many'), whereas in the voxel-driven approach, one would be measuring the contributions of all the LORs to a given voxel at a time ('many-to-one'). However, within the HRRT reconstruction framework, we have not seen this argument (which does not involve a proof) to actualize in experimental tests. We have in fact observed nearly similar results independent of whether the back-projection procedure is voxel-driven or LOR-driven, as elaborated shortly.

Due to the intrinsically LOR-based nature of list-mode reconstruction, only the LOR-driven projection operations may be utilized. This is one limitation of list-mode reconstruction, and is in a sense acquired due to the fact that one does not need to access the entire projection space in list-mode reconstruction (which is one important potential advantage of the technique in the first place, especially for low-statistic frames). In our reconstructions, as stated above and shown later, we have *not* observed a degradation in image quality when switching from voxel-driven back-projection (used in histogram mode) to LOR-driven back-projection.

In this work, three existing projection techniques were implemented and compared for use in list-mode reconstructions:

(1) *The Siddon method.* Following the work of Siddon (1985), this technique is based on calculating the path length of intersection of a given LOR along each voxel, as depicted in figure 4(a). However, we have experimentally demonstrated in this work that this technique, though very efficient in implementation, is considerably inferior in accuracy to the following two methods.

(2) *Trilinear interpolation.* To understand this technique, let us consider an image grid with voxels of unit length in all directions. Trilinear interpolation works by stepping through a given LOR with increments of unit length, as shown in figure 4(b) for the 2D case. For back-projection then one distributes the LOR value between the nearest voxels (four in 2D, eight in 3D). In forward-projection, similarly, the LOR value is obtained from the nearest eight (four) voxels in 3D (2D).

(3) *Bilinear interpolation.* In bilinear interpolation, the length of increments on a given LOR is chosen so as to ensure that the sampled points lie along the centres of the voxels in one direction, in order to eliminate interpolation in that direction. In our case, the dimension along which interpolation is eliminated is the transaxial (X or Y) direction along which

[8] By contrast, we have proposed in Rahmim *et al* (2004) an efficient *and* accurate motion correction EM algorithm that does not require the aforementioned randomized appraoch.

[9] Smoother bases (e.g., blobs) can also be used (Lewitt 1992). Blobs are spherically symmetric functions which handle interpolation issues more effectively than voxels. Moreover, use of splines, along with their very useful properties, seems to be a promising area of research, with regenerated interest in the recent years (Unser 1999). Voxels have the practical advantage of containing minimal support (i.e.,ño overlap), resulting in maximal sparseness in the system models, which in turn, relaxes computation times.

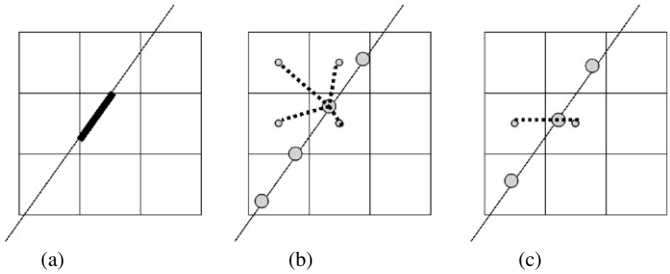

Figure 4. Projection algorithms employing (a) the Siddon method, (b) trilinear, and (c) bilinear interpolation techniques are drawn, as elaborated in the text.

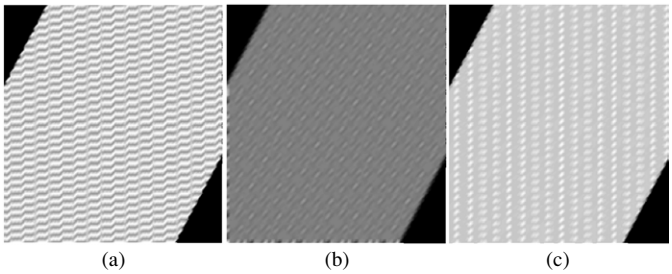

Figure 5. Results of back-projecting constant values along a projection direction onto a 64×64 image at axial $\theta = 0$ and transaxial $\phi = 30^\circ$. (a) Siddon, (b) trilinear and (c) bilinear.

the given LOR increases faster; e.g., Y direction for the LOR shown in figure 4(c). This method is potentially less accurate (which we have *not* observed to be the case, as shown later) than the trilinear counter-part since it makes the lengths of the increments LOR dependent. However, the technique is faster since: (i) interpolation along one direction is eliminated; i.e. for each point on the LOR, an interpolation is performed over only four (two) nearest voxels in 3D (2D) and (ii) for oblique LORs, fewer samples per LOR are considered.

The current implementation of the trilinear interpolation technique is $\sim$4 times slower than the Siddon method, while Bilinear interpolation is comparable (only $\sim$20% slower).

Figure 5 shows images obtained by back-projection of constant values along a projection direction at an oblique transaxial angle $\phi = 30$. Results are shown for the three aforementioned projection techniques. Horizontal profiles across these images can be used to compare the back-projection artefacts, as shown in figure 6(a). We have observed that the artefacts vary according to the projection angle, yet typically, the artefacts are seen to be stronger in the Siddon case as compared to the bilinear and trilinear interpolation techniques[10].

We shall also demonstrate in section 7.1 that (i) *reconstructed* image quality is manifestly superior when performing trilinear and bilinear interpolations, compared to the Siddon technique, while the two former techniques perform comparably and (ii) output-driven histogram-mode reconstruction yields nearly similar image qualities compared to LOR-driven list-mode reconstruction.

[10] The three methods are seen in figure 6(b) to perform nearly similarly in the forward-projection operation.

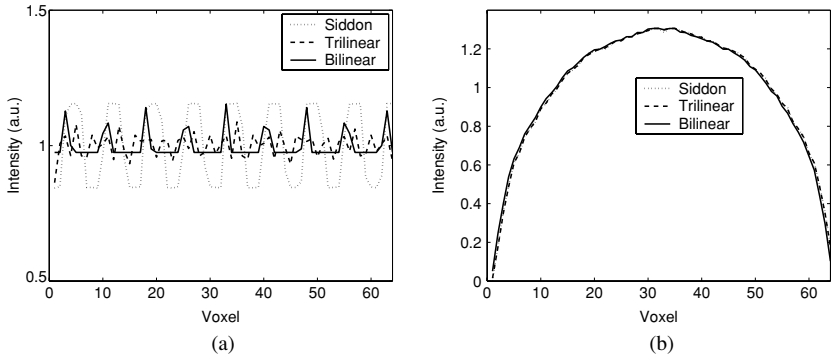

Figure 6. (a) Plots of horizontal profiles across the back-projection images depicted in figure 5. (b) Projection vector obtained with forward-projection of a uniform circle along $\theta = 0$ and $\phi = 15^\circ$.

6. Methods

6.1. Algorithms explored in this work

In this work, we implemented random- and scatter-corrected list-mode EM (LMEM) reconstructions, and investigated quantitative accuracy of these algorithms as well as the standard histogram-mode EM (HMEM) reconstruction schemes for state-of-the-art high-resolution dynamic PET imaging. Random (and scatter) subtraction techniques employing (i) sinogram non-negativity (SN) and (ii) image non-negativity (IN) constraints, as well as the OP-EM algorithm, were applied to data sets spanning a wide range of statistics. The algorithms considered can be summarized as follows:

(i) *Schemes without scatter correction*
FORE+2D-FBP: analytic image reconstruction without scatter correction;
RS-SN (random subtraction with the SN constraint);
RS-IN (random subtraction with the IN constraint).

(ii) *Schemes with scatter correction (SC)*
FORE+2D-FBP-SC: analytic image reconstruction with scatter correction;
RSS-SN-SC (random/scatter subtraction with the SN constraint[11]);
RS-IN-SC (random subtraction with the IN constraint; scatter estimates at denominator of EM equation);
OP-(LMEM or HMEM)-SC (random/scatter estimates at denominator of list-mode or histogram-mode EM equation).
The analytic FORE+2D-FBP reconstructions were used as gold standards for quantitative accuracy in dynamic reconstructions (due to the linearity property).

6.2. Tomograph: the HRRT

Data were acquired on the second generation of the high-resolution research tomographs (HRRT) (Wienhard *et al* 2002). This HRRT scanner has an octagonal design, with the detector heads consisting of a double 10 mm layer of LSO/LYSO for a total of 119 808

[11] The RS-SN-SC and RSS-IN-SC methods are not provided by the manufacturing company in the histogram-mode software. Note that the SN constraint is only applicable to histogram-mode reconstructions. The RSS method can also only be implemented in histogram mode, due to the smooth nature of scatter estimates which, unlike delayed coincidences as used in (22), cannot be appropriately used in the numerator of the list-mode EM algorithm.

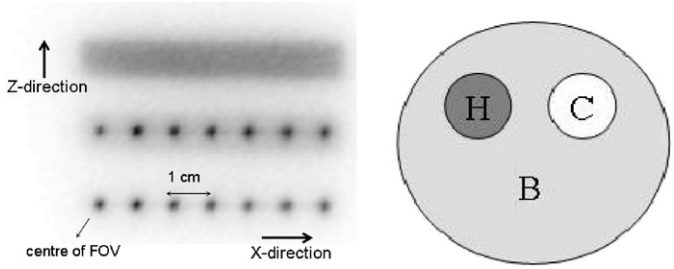

(a) (b)

Figure 7. (a) A sample reconstruction of the radioactive paper source (3 iterations and 16 subsets of the list-mode algorithm). The lower row of points sources as well as the rectangular box were utilized for analysis of resolution and noise properties. (b) Experimental contrast phantom used in this work.

detector crystals (crystal size $2.1 \times 2.1 \times 10$ mm^3). The total number of possible LORs is 4.486×10^9.

6.3. Experiment 1—radioactive paper source

This experiment was performed to study resolution and noise properties of the various projection techniques discussed in section (5.2). Using the technique presented in (Sossi *et al* 2005), which allows printing of radioactive patterns using a modified standard ink-jet printer, we imaged radioactive (^{18}F) point sources of size 0.7 mm placed at $X = 0, 1, 2, 3, 4, 5$ and 6 cm radially away from the centre of the FoV. The sample also included a 1×7 cm^2 rectangular area of uniform activity created for the purpose of monitoring noise behaviour. For better visualization, a sample reconstructed image of the radioactive paper source is shown in figure 7(a). The middle row of point sources (which were printed over a background) were not utilized for analysis in this work.

The overall FWHM for any given point was measured by calculation of the root-mean-squared value of the measured point widths in the transaxial (X, Y) and axial (Z) directions. The percentage noise (standard deviation/mean) for a given reconstructed image was calculated in two ways:

(1) *Voxel noise.* In which percentage variation of the individual voxels along the entire rectangle was measured.
(2) *ROI noise.* In which the activity rectangle was sub-divided into eight small rectangular ROIs and the percentage variation of the sum of counts in the ROIs was measured.

As elaborated in section 5.2, three LOR-driven projection methods were considered and implemented for performance of back- and forward-projection on the HRRT: (a) the Siddon method as well as (b) trilinear and (c) bilinear interpolation techniques. The data were subsequently reconstructed using the aforementioned projection methods (3 iterations and 16 subsets of the RS-IN list-mode algorithm were applied). Histogram-mode EM reconstruction was also applied to the data, wherein projection algorithms used bilinear interpolation and were output-driven (i.e., voxel-driven back-projection and LOR-driven forward-projection) as discussed in section 5.2. Subsequently, the resolution (FWHM) and noise properties of the reconstructed images were compared.

6.4. Experiment 2—contrast phantom

Phantom study. A 20 cm long, 10 cm radius phantom was used. The phantom had two 5 cm diameter cylindrical inserts, as depicted in figure 7(b), one was a 'cold' Teflon insert, and other was filled with a ^{11}C radioactivity concentration of 59.4 kBq ml^{-1} ('hot' insert). The phantom itself was filled with a ^{11}C concentration of 11.5 kBq ml^{-1} ('background'), yielding a hot insert to background ratio of 5.2. Eighteen dynamic frames (5 min each) were considered. The measurement thus covered 4.4 radioisotope half-lives. The random fraction was 25% in the first frame and 5% in the last frame.

Comparison schemes. The following comparisons were performed:

(i) *Time–activity curve (TAC) comparisons.* Plots of mean reconstructed voxel intensity (hot, cold and background regions) were obtained for all the reconstructed frames averaged over 40 transaxial planes.
(ii) *Axial profile comparisons.* Mean reconstructed voxel intensities within each axial plane (hot, cold and background regions) were plotted as a function of the axial plane. The corresponding curves for the various frames were overlaid for a visual comparison.
(iii) *Transaxial profile comparisons.* A line profile was placed along a summed transaxial plane (summed over 100 axial planes) through the hot spot and one of the cold spots. The transaxial profiles of the first frame (160M counts) were compared between the algorithms (4 iterations with 16 subsets).
(iv) *Contrast recovery comparisons.* The per cent contrasts for the hot and cold cylinders were calculated according to the NEMA NU 2001 protocol. The values were depicted as a function of the number of acquired counts per frame.
(v) *Noise comparisons.* The percentage noise was calculated as the ratio of the standard deviation of voxels distributed in the background region of the reconstructed image to the measured mean value. It was plotted as a function of iteration.

7. Results

7.1. Experiment 1—radioactive paper source

Figure 8 shows measured resolution values for the various points across the FoV[12], upon application of 3 iterations and 16 subsets of S-LMEM algorithm to the data. For comparison, results of application of histogram-mode EM reconstruction are also shown, wherein voxel-driven back-projection and LOR-driven forward-projection (referred to as output-driven projection) were used, as recommended by previous investigators (see discussion in section 5.2).

Similarly, noise versus iteration plots are shown in figure 9 for the aforementioned reconstruction algorithms, wherein (a) voxel noise and (b) ROI noise were considered, as described in section 6. Three main observations can be made with respect to these figures:

(1) Clearly, the Siddon technique performs noticeably poorly compared to the other interpolation methods (especially in terms of resolution).
(2) Trilinear and bilinear interpolation techniques perform nearly similarly.

[12] As a side note: one is also able to observe *space-variance* of the point spread function, manifesting itself as a degradation in resolution as one moves away from the centre of the FoV (seen in all the reconstruction tasks). This effect occurs due to a higher probability of inter-crystal penetration with higher angles of radiation incident on crystal fronts. Depth-of-interaction (DOI) encoding is known to improve this problem, but has not reached complete space-invariance.

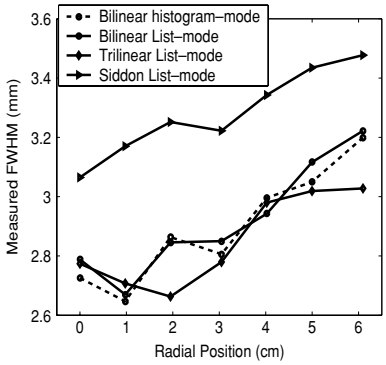

Figure 8. Plots of measured resolution versus radial position for the S-LMEM algorithm implemented using the Siddon algorithm as well as bilinear and trilinear interpolation techniques. For comparison, results of output-driven (as described in the text) histogram-mode OSEM reconstruction are also shown. Three iterations were performed.

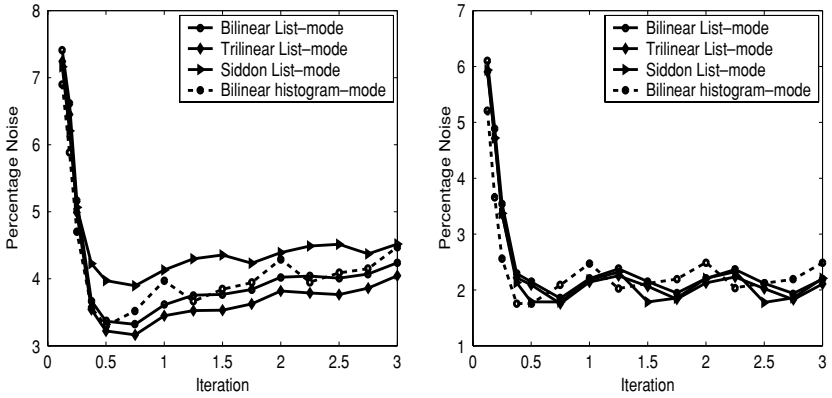

Figure 9. Plots of noise versus iteration for the reconstruction schemes described in the caption of figure 8. (a) Voxel noise and (b) ROI noise.

(3) Histogram-mode reconstruction with output-driven projections does not perform better than list-mode reconstruction with LOR-driven projections.

Given the aforementioned observations, and the fact that the current implementation of the trilinear interpolation technique is ∼4 times more expensive than the Siddon method, whereas bilinear interpolation is only around 20% slower, we are therefore prompted to select the bilinear technique as our method of choice in subsequent reconstructions.

7.2. Experiment 2—contrast phantom

TAC and axial profile comparisons. Figure 10 shows images of time–activity curves obtained for the three reconstruction schemes: (a) FORE+2D-FBP, (b) RS-IN and (c) RS-SN. The RS-IN algorithm is seen to yield a relatively flat TAC, similar to the FORE+2D-FBP case. However, the RS-SN scheme yields time–activity curves which (especially for the cold and background regions) increase with higher count-rate frames. This is attributed to the increasing

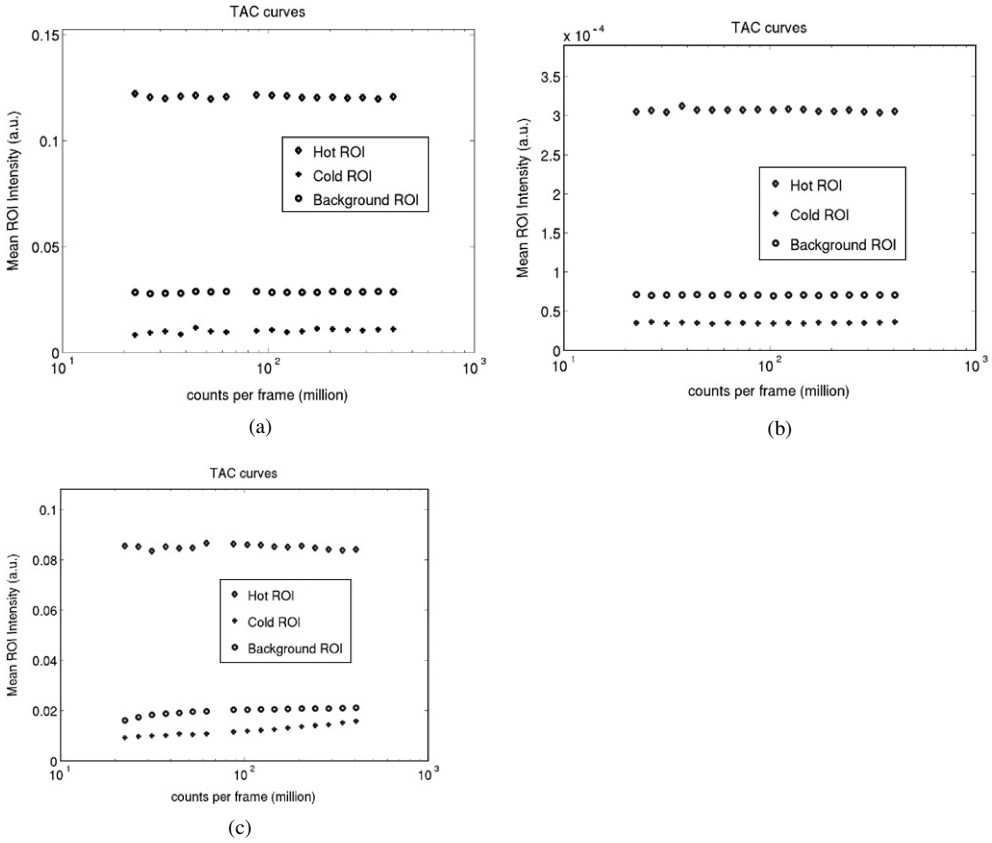

Figure 10. Time–activity curves (TACs) for 18 frames each 300 s in duration. First frame has a random fraction of 25%, last frame 5%. One iteration and 16 subsets are used in list-mode and OSEM reconstructions. (a) FORE+2D-FBP, (b) RS-IN and (c) RS-SN.

overestimation bias (when using SN constraint) with frames with higher random fractions (initial frames in the dynamic study).

Axial profiles of the mean ROI activity have been depicted in figure 11 for the hot (top), cold (bottom) and background (middle) regions. The profiles for the 18 frames have been drawn overlaying one another. The RS-IN algorithm is clearly seen to outperform the FORE+2D-FBP algorithm in terms of noise (especially in the background and cold regions). Furthermore, due to the aforementioned zero-thresholding bias, the RS-SN scheme does not yield overlapping axial profiles for the various frames and performs poorly.

Comparison of accelerated list-mode algorithms. Figures 12(a)–(c) show plots of percentage noise, as well as hot and cold contrasts for the OP-S-LMEM (with and without scatter correction) and the convergent OP-CS-LMEM algorithms. Clearly, even though the latter scheme relatively suppresses noise, it exhibits a very slow convergence rate in the cold region. We attribute this to the additive nature of the convergent algorithm (Rahmim *et al* 2004) resulting in a relatively slow update scheme. Furthermore, we observe the convergence rate to be relatively slow even in the ordinary subsetized algorithm such that using the hybrid ordinary/convergent algorithm will not noticeably improve the reconstruction task.

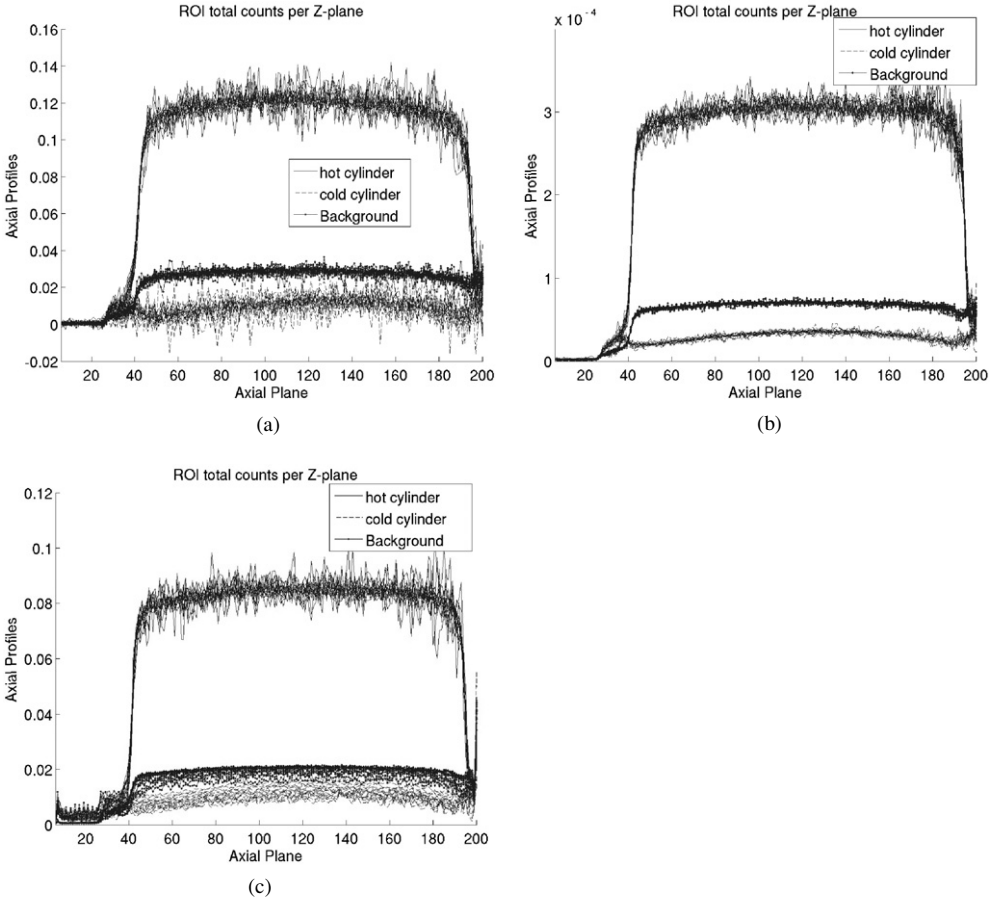

Figure 11. Axial profiles in the hot (top), cold (bottom) and background (middle) regions of the reconstructed images. (a) FORE+2D-FBP, (b) RS-IN and (c) RS-SN.

Subsequently, we have chosen to use the S-LMEM approach (where applicable) in the rest of this work.

Comparison of non-negativity constraints and the OP method. Figure 13(a) shows transaxial profiles through first frame of the data (161M total counts, 25% random fraction), reconstructed without scatter correction for the RS-SN, RS-IN and OP-LMEM schemes. Clearly, the sinogram non-negativity constraint (in RS-SN) results in an overestimation bias. On the other hand, use of image non-negativity (in RS-IN) removes this bias with respect to the OP-LMEM technique. In the case when scatter correction is applied, figure 13(b) shows similar profiles through images reconstructed using the scattered-corrected RSS-SN-SC, RS-IN-SC and OP-LMEM-SC algorithms. The histogram-mode OP-HMEM-SC algorithm (not shown) was also observed to nearly coincide with the latter two schemes. Here again, we note that the sinogram non-negativity constraint produces an overestimation bias with respect to the other methods and clearly exhibits degradation of contrast between the active and cold regions.

Figures 14(a) and (b) show TACs comparing the analytic FORE+2D-FBP-SC and statistical OP-LMEM-SC algorithms. A higher level of TAC variance is observed for the analytic technique, while also reconstructing negative values for the cold region, while the

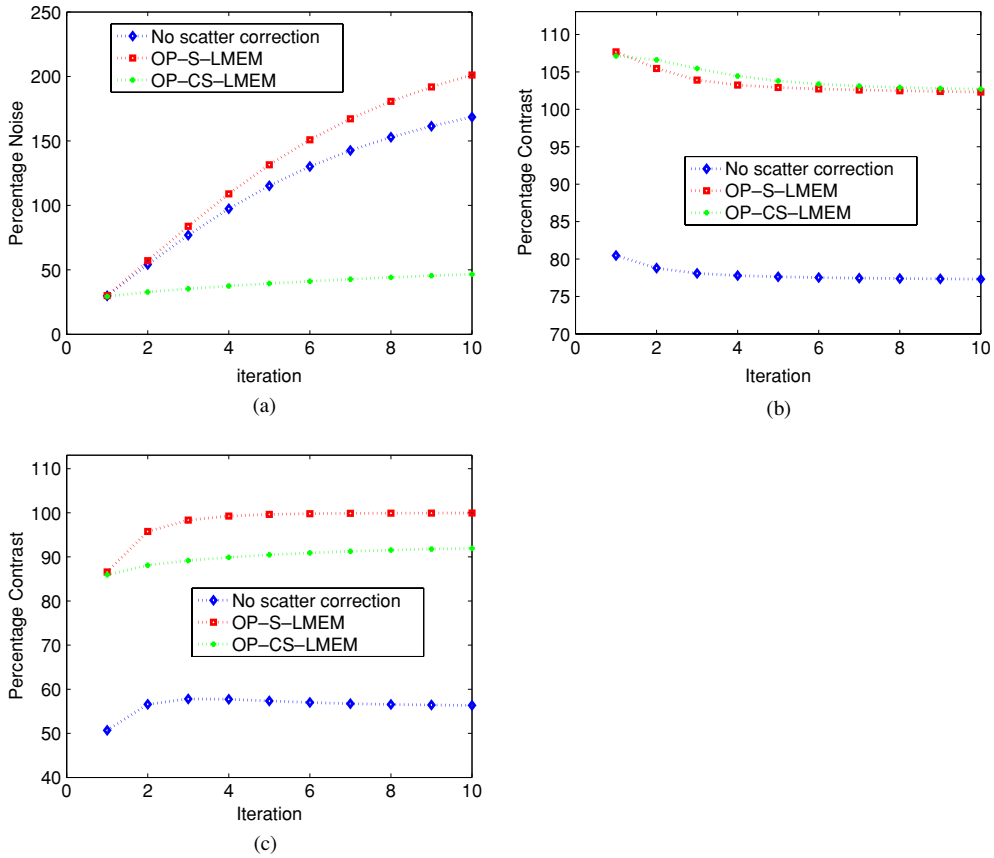

Figure 12. Plots of (a) percentage noise, as well as (b) hot and (c) cold contrasts for three reconstruction schemes. The frame included 32M counts.

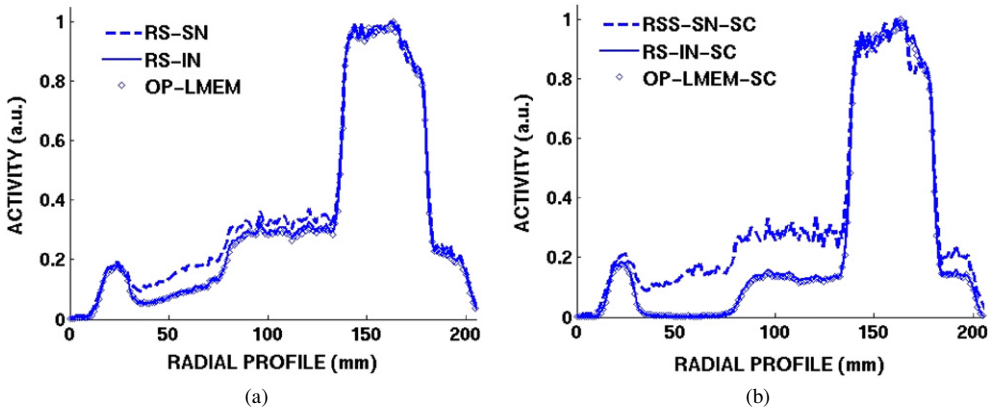

Figure 13. Transaxial plots comparisons (as described in section 6) between various reconstruction schemes (a) without and (b) with scatter correction. The frame included 32M counts.

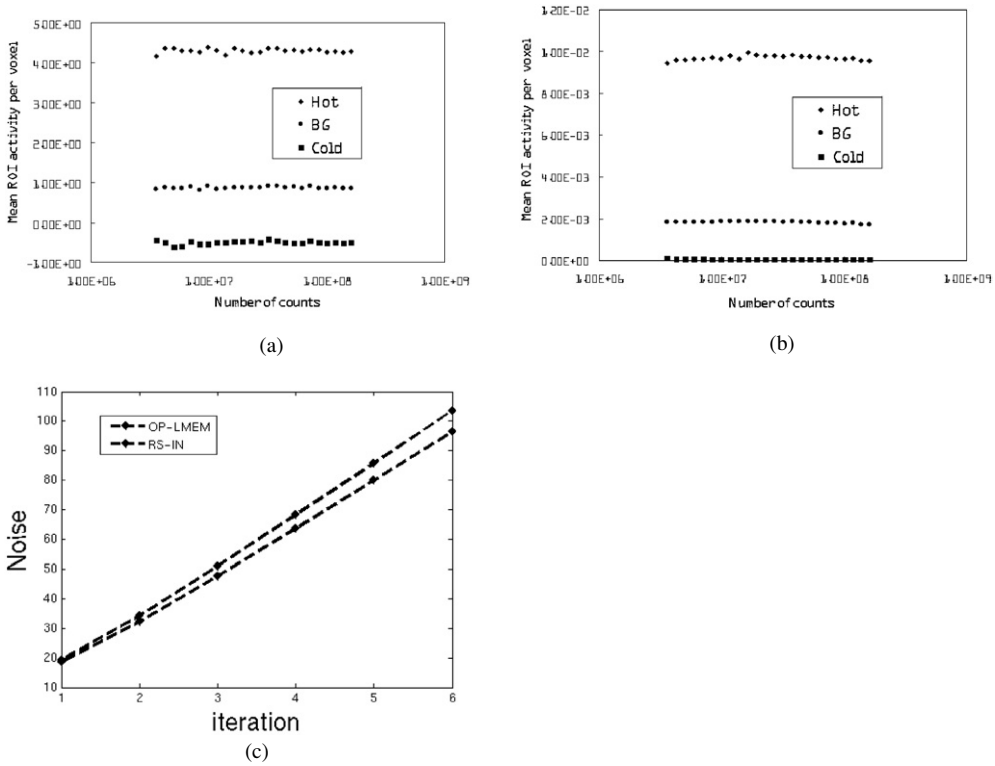

Figure 14. Time–activity curves for (a) FORE+2D-FBP-SC and (b) OP-LMEM-SC algorithms. The statistical list-mode approach clearly exhibits improved variance. Percentage noise comparisons between the list-mode RS-IN-SC and OP-SC algorithms are depicted in (c). The frame included 32M counts.

OP technique produces nearly uniform and non-biased TAC curves for a very wide range of statistics (TAC uniformity was also observed for the random-subtraction RS-IN method in figure 10(b).

Figure 14(c) compares the noise properties of the RS-IN-SC and OP-LMEM-SC algorithms. Clearly, while we have seen the IN constraint to remove the overestimation bias observed when using the SN constraint, it is seen here to exhibit a higher degree of noise compared to the OP-LMEM-SC scheme. This is attributed the exact Poisson nature of the prompts which are directly reconstructed using the OP approach.

As a last remark, we note that implementation of early termination of the iterative tasks in this work has been mainly for (i) computational complexity considerations as well as (ii) to suppress noise growth. The number of iterations used in the aforementioned studies may not be indicative of what will be required in actual animal and patient scans. In future works, we shall determine optimal stopping criteria by studying the convergence of measured counts in regions-of-interest used in modelling tasks.

8. Conclusion

High-resolution PET imaging imposes a number of challenges to the image reconstruction task, including that of increasingly large and sparse data sets. In this work, we have analysed

and addressed quantitative accuracy considerations in the particular context of state-of-the-art dynamic imaging:

(i) We have argued theoretically and shown experimentally that with the typical average number of events per LOR now (much) less than unity, the sinogram non-negativity constraint (when using the delayed-coincidence and/or scatter-subtraction techniques) is expected to result in considerable overestimation biases. This has been shown to particularly degrade contrast recovery and to adversely affect time–activity curves.

(ii) By contrast, techniques employing the milder *image* non-negativity constraints, as well as methods including the expected random and scatter estimates inside the reconstruction algorithms, are shown to resolve the bias, with the latter exhibiting preferable noise properties.

(iii) We have demonstrated that the accelerated list-mode image reconstruction method provides a very practical solution for efficient and quantitatively accurate reconstructions across a wide range of statistics for the HRRT scanner, rendering the technique very suitable for dynamic (4D) imaging in state-of-the-art high-resolution tomographs.

Acknowledgments

This work was supported by the Canadian Institute of Health Research, the TRIUMF Life Science Grant, the Natural Sciences and Engineering Research Council of Canada UFA (V Sossi) and University of British Columbia UGF (A Rahmim) scholarships, as well the Michael Smith Foundation for Health Research scholarship (V Sossi). Part of the computation was performed on the Western Canada Research Grid, for which the authors wish to express gratitude. The authors wish to especially thank Dr Kelvin Raywood for his continuous support particularly in regards to facilitation of the group's parallel-computing cluster.

References

Ahn S and Fessler J A 2004 Emission image reconstruction for randoms-precorrected PET allowing negative sinogram values *IEEE Trans. Med. Imaging* **23** 591–601

Badawi R D, Miller M P, Bailey D L and Marsden P K 1999 Randoms variance-reduction in 3D-PET *Phys. Med. Biol.* **44** 941–54

Bailey D L and Jones T 1994 A convolution-subtraction scatter correction method for 3D PET *Phys. Med. Biol.* **39** 411–24

Barker W C, Liow J-S, Zhao Y, Thada S, Iano-Fletcher A, Lenox M, Michel C, Johnson C A and Carson R E 2004 Randoms estimation for list-mode reconstruction for the ECAT HRRT *IEEE NSS & MIC 2004 Conf. Rec. (Rome, Oct. 2004)*

Bélanger M-J, Mann J J and Parsey R V 2004 OS-EM and FBP reconstructions at low count rates: effect on 3D PET studies of [^{11}C] WAY-100635 *Neuroimage* **21** 244–50

Byrne C 1998 Iterative algorithms for deblurring and deconvolution with constraints *Inverse Problems* **14** 1455–67

Carson R E, Barker W C, Liow J-S and Johnson C A 2003 Design of a motion-compensation OSEM list-mode algorithm for resolution-recovery reconstruction for the HRRT *IEEE Nucl. Sci. Symp. Conf. Rec.* **5** 19–25, 3281–5

Casey M E and Hoffman E J 1986 Quantitation in positron emission tomography: 7. A technique to reduce noise in accidental coincidence measurements and coincidence efficiency calibration *J. Comput. Assist. Tomogr.* **10** 845–50

Cherry S R, Meikle S and Hoffman E J 1993 Correction and characterization of scattered events in 3D PET using scanners with retractable septa *J. Nucl. Med.* **34** 671–8

Daube-Witherspoon M E *et al* 2002 PET performance measurements using NEMA 2-2001 standard *J. Nucl. Med.* **43** 1398–409

Egger M 1996 Fast volume reconstruction in positron emission tomography: implementation of four algorithms on a high performance scalable parallel platform *PhD Dissertation* University of Lausanne, Switzerland

Erlandsson K, Visvikis D, Waddington W A, Cullum I, Jarritt P H and Pilowsky L S 2000 Low-statistics reconstruction with AB-EMML *IEEE Nucl. Sci. Symp. Conf. Rec.* **2** 249–53

Fessler J A 1994 Penalized weighted least-sqaures image reconstruction for positron emission tomography *IEEE Trans. Med. Imaging* **13** 290–300

Grootoonk S, Spinks T J, Sashin D, Spyrou N M and Jones T 1996 Correction for scatter in 3D brain PET using a dual energy window method *Phys. Med. Biol.* **41** 2757–74

Hebert T J and Leahy R 1990 Fast methods for including attenuation in the EM algorithm *IEEE Trans. Nucl. Sci.* **37** 754–8

Hsiao I T, Rangarajan A and Gindi G 2002a A provably convergent OS-EM like reconstruction algorithm for emission tomography *Conf. Rec. SPIE Med. Imaging* **4684** 10–9

Hsiao I T, Rangarajan A and Gindi G 2002b A new convergent MAP reconstruction algorithm for emission tomography using ordered subsets and separable surrogates *Conf. Rec. IEEE Int. Symp. Biomed. Imaging* 409–12

Hudson H M and Larkin R S 1994 Accelerated image reconstruction using ordered subsets of projection data *IEEE Trans. Med. Imaging* **13** 601–9

Khurd P K and Gindi G R 2003 A Globally convergent ordered-subset algorithm for list-mode reconstruction *IEEE NSS & MIC Conf. Rec. (Portland, OR; Oct. 2003)*

Kimdon J A, Qi J and Moses W W 2003 Effect of random and scatter fractions in variance reduction using time-of-flight information *IEEE NSS & MIC Conf. Rec. (Portland, OR, Oct. 2003)*

Kohli V, King M A, Byrne C, Gifford H C and Narayan M N 1999 AB-EMML iterative reconstruction algorithm incorporating upper and lower bounds for accelerating resolution recovery in SPECT imaging *Proc. 1999 Int. Meeting Fully Three-Dimensional Image Reconst. in Radiol. and Nucl. Med.* pp 212–5

Leahy R M and Qi J 2000 Statistical approaches in quantitative positron emission tomography *Stat. Comput.* **10** 147–65 (invited paper)

Lewitt R M 1992 Alternatives to voxels for image representation in iterative reconstruction algorithms *Phys. Med. Biol.* **37** 707–16

Markiewicz P J, Reader A J, Tamal M, Julyan P J and Hastings D L 2004 Towards an analytic unified scatter and attenuation system model for 3D whole body PET imaging *IEEE NSS & MIC 2004 Conf. Rec. (Rome, Oct. 2004)*

Michel C, Liu X, Sanabria S, Lonneux M, Sibomana M, Bol A, Comtat C, Kinahan P E, Townsend D W and Defrise M 1999 Weighted schemes applied to 3D-OSEM reconstruction in PET *IEEE Nucl. Sci. Symp. Conf. Rec.* **3** 1152–7

Michel C, Sibomana M, Boi A, Bernard X, Lonneux M, Defrise M, Comtat C, Kinahan P E and Townsend D W 1998 Preserving Poisson characteristics of PET data with weighted OSEM reconstruction *IEEE Nucl. Sci. Symp. Conf. Rec.* **2** 1323–9

Moses W W 2003 Time of flight in PET revisited *IEEE Trans. Nucl. Sci.* **50** 1325–30

Mumcuoğlu E Ü, Leahy R M and Cherry S R 1996a Baysian reconstruction of PET images: methodology and performance analysis *Phys. Med. Biol.* **41** 1777–807

Mumcuoğlu E Ü, Leahy R M, Cherry S R and Hoffman E 1996b Accurate geometric and physical response modelling for statistical image reconstruction in high resolution PET *IEEE Nucl. Sci. Symp. Conf. Rec.* **3** 1569–73

Narayanan M V, King M A, Soares E J, Byrne C L, Pretorius P H and Wernick M N 1999 Application of the Karhunen–Loéeve transform to 4D reconstruction of cardiac gated SPECT images *IEEE Trans. Nucl. Sci.* **46** 1001–8

Nichols T E, Qi J, Asma E and Leahy R M 2002 Spatiotemporal reconstruction of list-mode PET data *IEEE Trans. Med. Imaging* **21** 396–404

Nutt R 2003 *History of PET* www.cpspet.com/our_company/history_o_pet.shtml (For a different perspective on the early history of PET, the reader is recommended to consult: Brownell G L *A History of Positron Imaging* www.mit.edu/∼glb/alb.html)

Ollinger J M 1996 Model-based scatter correction for fully 3-D PET *Phys. Med. Biol.* **41** 153–76

Parra L and Barrett H H 1998 List-mode likelihood: EM algorithm and image quality estimation demonstrated on 2-D PET *IEEE Trans. Med. Imaging* **17** 228–35

Politte D G and Snyder D L 1991 Corrections for accidental coincidences and attenuation in maximum-likelihood image reconstruction for positron-emission tomography *IEEE Trans. Med. Imaging* **10** 82–9

Qi J and Huesman R H 2003 Propagation of errors from the sensitivity image in list mode reconstruction *IEEE NSS & MIC 2004 Conf. Rec. (Portland, OR, Oct. 2003)*

Rahmim A, Bloomfield P, Houle S, Lenox M, Michel C, Buckley K R, Ruth T J and Sossi V 2004 Motion compensation in histogram-mode and list-mode EM reconstructions: beyond the event-driven approach *IEEE Trans. Nucl. Sci.* **51** 2588–96

Rahmim A, Lenox M, Reader A J, Michel C, Burbar Z, Ruth T J and Sossi V 2004 Statistical list-mode image reconstruction for the high resolution research tomograph *Phys. Med. Biol.* **49** 4239–58

Reader A J 1999 Image reconstruction and correction techniques for positron volume imaging with rotating planar detectors *PhD Dissertation* University of London

Reader A J, Ally S, Bakatselos F, Manavaki R, Walledge R, Jeavons A P, Julyan P J, Zhao S, Hastings D L and Zweit J 2002 One-pass list-mode EM algorithm for high-resolution 3-D PET image reconstruction into large arrays *IEEE Trans. Nucl. Sci.* **49** 693–9

Reader A J, Erlandsson K, Flower M A and Ott R J 1998 Fast accurate iterative reconstruction for low-statistics positron volume imaging *Phys. Med. Biol.* **43** 835–46

Reader A J, Zhao S, Julyan P J, Hastings D L and Zweit J 2001 Adaptive correction of scatter and random events for 3-D backprojected PET data *IEEE Nucl. Sci. Trans.* **48** 1350–6

Rokitta O, Casey M, Wienhard K and Pictrzyk U 2000 Random correction for positron emission tomography using singles count rates *IEEE Nucl. Sci. Symp. Conf. Rec.* **3** 17/37–17/40

Siddon R L 1985 Fast calculation of the exact radiological path for a three-dimensional CT array *Med. Phys.* **12** 252–5

Snyder D L, Helstrom C W, Lanterman A D, Faisal M and White R L 1995 Compensation for readout noise in CCD images *J. Opt. Soc. Am.* A **12** 272–83

Sossi V, Buckley K R, Piccioni P, Rahmim A, Camborde M-L, Strome E, Lapi S and Ruth T J 2005 Printed sources for positron emission tomography (PET) *Trans. Nucl. Sci.* **52** 114–8

Tamal M, Reader A J, Markiewicz P J, Hastings D L and Julyan P J 2004 Noise properties of four strategies for incorporation of scatter and attenuation information in 3D whole body PET *IEEE NSS & MIC Conf. Rec. (Rome, Oct. 2004)*

Unser M 1999 Splines: a perfect fit for signal and image processing *IEEE Signal Process. Mag.* **16** 22–38

Wallis J W and Miller T R 1997 An optimal rotator for iterative reconstruction *IEEE Trans. Med. Imaging* **16** 118–23

Watson C C 2000 New, faster, image-based scatter correction for 3D PET *IEEE Trans. Nucl. Sci.* **47** 1587–94

Watson C C 2003 The ECAT HRRT: an example of NEMA scatter estimation issues for LSO based PET systems *IEEE NSS & MIC Conf. Rec. (Portland, OR, Oct. 2003)*

Wienhard K *et al* 2002 The ECAT HRRT: performance and first clinical application of the new high resolution research tomograph *IEEE Trans. Nucl. Sci.* **49** 104–10

Yavuz M 1999 Statistical tomographic image reconstruction methods for randoms-precorrected PET measurements *PhD Dissertation* University of Michigan, Ann Arbor

Yavuz M and Fessler J A 1996 Objective functions for tomographic reconstruction from randoms-precorrected PET scans *Proc. IEEE Nuclear Science Symposium and Medical Imaging Conference (Anaheim, CA)* vol 2 pp 1067–71

Yavuz M and Fessler J A 1998 Statistical image reconstruction methods for randoms-precorrected PET scans *Med. Image Anal.* **2** 369–78